



High-entropy perovskite oxides: A versatile class of materials for nitrogen reduction reactions

Kaibin Chu¹, Jingjing Qin¹, Haiyan Zhu¹, Michiel De Ras², Chuang Wang², Lei Xiong³, Longsheng Zhang¹, Nan Zhang¹, Johan A. Martens⁴, Johan Hofkens^{2,5}, Feili Lai^{2*} and Tianxi Liu^{1*}

ABSTRACT Despite the intense research efforts directed to electrocatalytic nitrogen reduction reaction (eNRR), the NH₃ yield and selectivity are still not up to the standard of practical application. Here, high-entropy perovskite oxides with composition Ba_x(FeCoNiZrY)_{0.2}O_{3-δ} (B_x(FCNZY)_{0.2} (x = 0.9, 1) are reported as eNRR catalysts. The eNRR activity of high-entropy perovskite oxide is enhanced by changing the nonstoichiometric metal elements at the A-site, thus generating additional oxygen vacancies. The NH₃ yield and Faraday efficiency for B_{0.9}(FCNZY)_{0.2} are 1.51 and 1.95 times higher than those for B(FCNZY)_{0.2}, respectively. The d-band center theory is used to theoretically predict the catalytically active center at the B-site, and as a result, nickel was identified as the catalytic site. The free energy values of the intermediate states in the optimal distal pathway show that the third protonation step (*NNH₂ → *NNH₃) is the rate-determining step and that the increase in oxygen vacancies in the high-entropy perovskite contributes to nitrogen adsorption and reduction. This work provides a framework for applying high-entropy structures with active site diversity for electrocatalytic nitrogen fixation.

Keywords: high entropy, perovskite, nitrogen reduction reaction, catalytic activity center

INTRODUCTION

Nitrogen is of great importance to all life forms [1,2]. However, nitrogen in nature cannot be used directly by most species, including humans, and thus must be converted into reactive nitrogen-containing compounds (e.g., NH₃ and HNO₃). Although the industrial synthesis of NH₃, mostly *via* the Haber-Bosch (H-B) process, has satisfied the needs for societal development over the past century, it also has an irreversible environmental effect due to the typical harsh conditions for the H-B process (e.g., high temperature of 400–600°C and high pressure of 15–30 MPa), the resulting large energy consumption, and the subsequent emission of greenhouse gases [3–5]. Therefore, new methods for NH₃ synthesis under mild conditions must be developed to realize the goals for carbon neutrality and peak

CO₂ emissions [6–12]. Electrocatalytic nitrogen reduction reaction (eNRR) has attracted global attention because of its renewable feedstocks (nitrogen and water), mild reaction conditions, and simple infrastructure [13–17]. With progress in this field, electrocatalytic materials have gradually expanded from the initial precious metal materials to non-precious metal catalysts abundant in nature. However, the rational design of electrocatalytic materials with high NH₃ yield and selectivity remains a challenge due to the inertness of the N≡N bond that is difficult to break and the presence of competitive hydrogen evolution reaction (HER) for aqueous electrolytes. Therefore, all mechanistic aspects of nitrogen reduction must be comprehensively understood to enhance the electrochemical activity for NH₃ generation [18–23]. Owing to their unique compositional and structural flexibility [24], perovskite oxides have been explored as candidate materials for eNRR and have shown great promise in catalytic activity and stability [18,19,25–32]. Sun's group [25] reported porous LaFeO₃ nanofibers as an efficient eNRR catalyst with a Faradaic efficiency (FE) of 8.77% and a good NH₃ yield rate of 18.59 μg h⁻¹ mg_{cat.}⁻¹ at -0.55 V. The eNRR activity of perovskite materials can also be enhanced by heteroatom doping (e.g., Cs and Ni) [28]. Despite these potential advantages of perovskites for eNRR, the construction of perovskite-type electrocatalytic materials with sufficient active sites for N₂ adsorption and reduction remains a great challenge.

High-entropy (HE) materials show potential application in electrocatalysis, including electrochemical reactions, due to their intrinsic abundant active sites, complex electronic structures, and random element distributions. The concept of mixed entropy (ΔS_{mix}) was first introduced in the field of materials science in 2004 [33]. ΔS_{mix} can be expressed as the following Gibbs formula: $\Delta S_{\text{mix}} = -R \sum_{i=1}^N c_i \ln c_i$, where R is the ideal gas constant, N is the number of elements, and c_i is the atomic fraction of component i . A material is considered to have high entropy when its ΔS_{mix} is higher than 1.5R. On this basis, a series of HE materials have been developed (e.g., HE halides [34], carbides [35], nitrides [36], sulfides [37], borides [38], oxides [39], and phosphate [40]) and employed as promising electrocatalysts. Among available HE materials, HE perovskites (HEPs),

¹ The Key Laboratory of Synthetic and Biological Colloids, Ministry of Education, School of Chemical and Material Engineering, International Joint Research Laboratory for Nano Energy Composites, Jiangnan University, Wuxi 214122, China

² Department of Chemistry, KU Leuven, Celestijnenlaan 200F, Leuven 3001, Belgium

³ State Key Laboratory of Food Science and Technology, Jiangnan University, Wuxi 214122, China

⁴ Centre of Surface Chemistry and Catalysis: Characterisation and Application Team, KU Leuven, Leuven 3001, Belgium

⁵ Max Planck Institute for Polymer Research, Ackermannweg 10, Mainz 55128, Germany

* Corresponding authors (emails: feili.lai@kuleuven.be (Lai F); txliu@jiangnan.edu.cn (Liu T))

especially HE perovskite oxides, have recently received interest in electrocatalysis application because of their tunable constituent elements, various active sites, and structural stability. A mechanochemical method was used to synthesize perovskite oxide-fluoride solid solutions with ultra-high entropy values and remarkably enhanced electroactivities for oxygen evolution reaction compared with the corresponding perovskite oxide precursors [41]. Although HEPs have more versatile electronic structures and active sites than conventional perovskites, the former have never been applied in eNRR, making them an interesting subject for the discovery of highly active materials for eNRR research. Introducing additional oxygen vacancies in the structure of HE perovskite oxides appears to be an interesting path to exploit this structural feature in eNRR and further utilize the complexity and diversity of B-sites in these materials. In perovskite structures, oxygen vacancy has a direct impact on the crystal structure, electronic properties, and chemical environment at the surface. Hence, oxygen vacancies are important in promoting the electrocatalytic activities of perovskite oxides. Over the past decade, important progress has been achieved with the use of oxygen vacancies in the rational design of perovskite materials exhibiting excellent oxygen reduction reaction (ORR) performance. Oxygen vacancies can be generated by A-site cation non-stoichiometry, such as $(\text{Ba}_{0.5}\text{Sr}_{0.5})_{1-x}\text{Co}_{0.8}\text{Fe}_{0.2}\text{O}_{3-\delta}$, $\text{La}_{1/3}\text{NbO}_3$, $\text{Sr}_{0.95}\text{Nb}_{0.1}\text{Co}_{0.9}\text{O}_{3-\delta}$, and $\text{La}_{1-x}\text{FeO}_{3-\delta}$ [42,43]. For example, $\text{Sr}_{0.95}\text{Nb}_{0.1}\text{Co}_{0.9}\text{O}_{3-\delta}$ with A-site cation non-stoichiometry exhibits superior ORR activities compared with its parent stoichiometric material because of the high oxygen vacancy concentration and resulting electrical conductivity [44]. Metals Fe, Co, Ni, Zr, and Y are typical centers for the B-site [45]; Fe, Co, and Ni are regarded as nitrogen-reducing sites [19,28,32]; and Zr and Y have a positive effect on suppressing the competing HER [46]. However, HEPs have never been systematically investigated as model systems in the electrocatalysis of eNRR and HER.

Herein, we synthesized HEP of $\text{Ba}_x(\text{FeCoNiZrY})_{0.2}\text{O}_{3-\delta}$ ($\text{B}_x(\text{FCNZY})_{0.2}$) using a modified sol-gel method. The resulting lava-like HEP solid with additional oxygen vacancies and modified electric structure of B-site metals (obtained by controlling nonstoichiometric metal element at the A-site) exhibits an improved eNRR performance. $\text{B}_{0.9}(\text{FCNZY})_{0.2}$ with additional oxygen vacancies shows enhanced NH_3 yield rate and corresponding FE compared with $\text{B}(\text{FCNZY})_{0.2}$. The enhanced eNRR activity of $\text{B}_{0.9}(\text{FCNZY})_{0.2}$ is attributed to the additional oxygen vacancies and synergistic effect among various metal elements in the B-site, which will be discussed in detail through density functional theory (DFT) calculations.

EXPERIMENTAL SECTION

Synthesis of chopped pre-oxidized polyacrylonitrile (oPAN) nanofibers

First, 1 g of PAN powder was dissolved in 10 mL of dimethyl formamide (DMF) solution for 24 h. The homogeneous solution was then loaded into a syringe with a steel nozzle (23G). A high voltage of 17 kV was applied between the collector and needle tip at 13 cm. The as-spun membranes were pre-oxidized at 200°C for 2 h. Finally, 360 mg of the oPAN nanofibers in 80 mL of aqueous solution was mechanically shredded using a dispersion machine at $13,000 \text{ r min}^{-1}$ for 0.5 h to form a homogeneous dispersion.

Synthesis of porous lava-like HE perovskite oxides

$\text{Ba}_x(\text{FeCoNiZrY})_{0.2}\text{O}_{3-\delta}$ ($x = 0.9, 1$)

The samples of $\text{Ba}_x(\text{FeCoNiZrY})_{0.2}\text{O}_{3-\delta}$ ($\text{B}_x(\text{FCNZY})_{0.2}$) were prepared by a modified sol-gel method. Here, $\text{B}(\text{FCNZY})_{0.2}$ was used as an example. The six metal nitrates at a certain molar ratio according to the targeted material formula ($\text{Ba:Fe:Co:Ni:Zr:Y} = 2:0.4:0.4:0.4:0.4:0.4$ (mmol)), were dissolved in 100 mL of deionized water. Certain amounts of ethylene glycol (EG) and citric acid (CA) at a molar ratio of 3:1.5:1 (EG:CA:total metal cations) were prepared as a single solution, which was subsequently poured into the mixed metal nitrate solution to create chelation between EG/CA and the metal cations. For complete complexation, the pH value of the solution was adjusted to ~ 9 by adding ammonium hydroxide. Under magnetic stirring and heating at 80°C, the water in the solution was slowly evaporated to form a dark yellow gel. In brief, 5 mL of the homogeneous dispersion of chopped pre-oPAN nanofibers was slowly added dropwise to the gel. The mixed gel was heated to ensure that the viscosity remained constant until all drops were added to form a uniformly dispersed gel. The resulting gel was then aged at 200°C for 5 h to form the precursor, which was then further sintered at 1000°C for 5 h to remove the organic substance and form the phase of HE perovskite oxides. The synthesis method for perovskite $\text{B}_{0.9}(\text{FCNZY})_{0.2}$ was similar, except the molar ratio of metals was changed to $\text{Ba:Fe:Co:Ni:Zr:Y} = 1.8:0.4:0.4:0.4:0.4:0.4$.

Cathode preparation

Approximately 6 mg of $\text{B}_x(\text{FCNZY})_{0.2}$ and 60 μL of Nafion solution (5 wt%) were dispersed in 1940 μL of absolute ethyl alcohol and sonicated to form a homogeneous ink. Afterward, 40 μL of the above ink was loaded onto a carbon paper electrode (CPE) with an area of $1 \text{ cm} \times 1 \text{ cm}$ and dried in an Ar atmosphere at 80°C for 1 h.

Characterization

X-ray diffraction (XRD) patterns were collected on a Bruker D8 X-ray diffractometer with a Cu K α X-ray source ($\lambda = 1.5418 \text{ \AA}$). High-resolution transmission electron microscopy (HRTEM) was performed using a JEOL JEM-2100Plus electron microscope. Scanning electron microscopy (SEM) was carried out on a HITACHI S-4800 electron microscope. X-ray photoelectron spectroscopy (XPS) and valence band measurements were carried out with an AXIS Supra. Electron paramagnetic resonance (EPR) spectra were measured using an EPR spectrometer (Bruker A300). Inductively coupled plasma mass spectrometry (ICP-MS) was conducted on a Thermo Fisher Scientific Inc ICAP TQ instrument. Ion chromatography (IC) was performed with a Thermo Scientific Dionex ICS-5000 IC instrument. $^{14}\text{NH}_4^+$ and $^{15}\text{NH}_4^+$ electrolytes were determined by ^1H nuclear magnetic resonance (NMR) using an AVANCE3HD600MHZ instrument. Specific surface area values were measured by the Brunauer-Emmett-Teller (BET) method using Autosorb-IQ3.

Electrochemical measurements

Electrochemical tests were carried out under an H-shaped electrolytic cell with a three-electrode system with 0.1 mol L^{-1} lithium sulfate solution as the electrolyte, HEP-loaded CPE (HEP/CPE) as the working electrode, graphite electrode as the counter electrode, and saturated Ag/AgCl electrode as the reference electrode. The electrolytes in the cell were separated

using a Nafion 117 membrane treated as previously described [32]. All potentials were converted to the potential of the relatively reversible hydrogen electrode (RHE) using the formula (E (vs. RHE)) = E (vs. Ag/AgCl) + 0.197 + 0.059 × pH). Linear sweep voltammetry (LSV) curves were scanned in the range from -1.0 to 0 V. Some control experiments were also carried out under the following conditions: (i) potentiostatic measurements of $B_{0.9}(\text{FCNZY})_{0.2}$ in the Ar-saturated electrolyte, (ii) open-circuit tests of $B_{0.9}(\text{FCNZY})_{0.2}$ in the N_2 -saturated electrolyte, and (iii) potentiostatic measurements of pure carbon paper in the N_2 -saturated electrolyte. Cyclic voltammetry curves were scanned under a potential window between 1.0 and 1.1 V. The double-layer capacitance (C_{dl}) is the slope obtained by fitting these data for sweep speed and current density at 1.05 V. Electrochemical impedance spectroscopy (EIS) was measured at -0.6 V from 0.1 Hz to 100 kHz.

Determination of NH_3 and N_2H_4

The concentration of the produced NH_3 in the electrolyte was spectrophotometrically measured by the indophenol blue method [47]. In brief, 2 mL of 1 mol L^{-1} NaOH solution containing salicylic acid (5 wt%) and sodium citrate (5 wt%) was added, followed by 1 mL of NaClO solution (0.05 mol L^{-1}) and 0.2 mL of sodium nitroferricyanide solution (1 wt%). Absorbance measurements were performed from 550 to 750 nm. The concentration-absorbance (at 655 nm) curve was calibrated using a standard NH_4^+ solution with a series of concentrations.

The amount of N_2H_4 present in the electrolyte was measured using the method of Watt and Chrisp [48]. The mixture of $\text{C}_9\text{H}_{11}\text{NO}$ (5.99 g), $\text{C}_2\text{H}_5\text{OH}$ (300 mL), and HCl (30 mL) was used as a color reagent. In brief, 5 mL of electrolyte was mixed with 5 mL of the as-prepared color reagent. After being stirred for 10 min at room temperature, the absorbance of the resulting solution was measured at a wavelength of 455 nm.

Calculations of NH_3 formation rate and FE

NH_3 formation rate was calculated using the following equation:

$$\text{NH}_3 \text{ formation rate} = [\text{NH}_4^+] \times V / (m_{\text{cat.}} \times t).$$

FE was calculated according to the following equation:

$$\text{FE} = 3 \times F \times [\text{NH}_4^+] \times V / (17 \times Q),$$

where $[\text{NH}_4^+]$ is the measured NH_4^+ concentration, V is the volume of the cathodic reaction electrolyte, t is the potential applied time, $m_{\text{cat.}}$ is the loaded quality of catalyst, F is the Faraday constant, and Q is the quantity of applied electricity.

Computational methods

DFT calculations were implemented with Vienna *ab initio* simulation package [49,50], where the Perdew-Burke-Ernzerhof generalized gradient approximation [51,52] and the projected augmented wave (PAW) [53] were used to describe the exchange/correlation potential and the ion-electron interaction, respectively. Cutoff energy of 600 eV was adopted for the plane-wave expansion of the electron wave function in all calculations. The vacuum space was set at least 20 \AA to separate the interactions between the neighboring slabs. For this calculation, a $5 \times 5 \times 1$ k -point mesh was adopted. Convergence criteria were set as 10^{-5} eV and 10^{-2} eV \AA^{-1} for the self-consistent field and ion steps, respectively. Grimme DFT-D3 dispersion correction method was also employed to accurately describe the weak van der Waals interactions [54]. The free energy diagram was plotted at $U = 0$ V as $\Delta G = \Delta E + \Delta \text{ZPE} - T\Delta S + eU$, where ΔE is the

electronic energy difference, ΔZPE is the change in zero-point energies, T is the temperature ($T = 298.15$ K), and ΔS is the entropy change. The entropy of H is $\Delta S_{\text{H}} \approx 0.5S_{\text{H}_2}^0$, where $S_{\text{H}_2}^0$ is the entropy of H_2 in the gas phase at standard conditions. Entropy data for H, NH_3 , and N_2 were collected from NIST (<https://www.nist.gov>). The entropies for adsorbed structures or intermediates were neglected because these samples are solid. Other details for NRRs can be found in previous research [55].

RESULTS AND DISCUSSION

Material synthesis and characterization

$B_x(\text{FCNZY})_{0.2}$ ($x = 0.9, 1$) was prepared by a liquid phase method, in which six metal (Ba, Fe, Co, Ni, Zr, and Y) precursors with chosen stoichiometric ratios were dissolved to form a uniform solution. Abundant chopped nanofibers were also prepared to generate a dispersion, which was then used as a polymer template to construct lava-like porous structures inside the HEPs. The preparation of porous lava-like HEPs with the formulation of $B_x(\text{FCNZY})_{0.2}$ ($x = 0.9, 1$) can be divided into three steps (Fig. 1a). First, the oPAN nanofibers (Fig. S1a) were mechanically chopped to an average diameter of ~ 300 nm (Fig. S1b). Second, the nitrates of the six metals were dissolved with a certain ratio and further chelated with CA and EG to obtain a yellow transparent solution, which was slowly evaporated to form a dark yellow gel. Third, the abundant chopped oPAN nanofibers were subjected to appropriate heating and stirring to generate a gel with uniformly dispersed chopped nanofibers. After the solvent was removed completely, $B_x(\text{FCNZY})_{0.2}$ ($x = 0.9, 1$) was finally obtained by high-temperature calcination. The synthesis method for $B_x(\text{FCNZY})_{0.2}$ ($x = 0.9, 1$) was identical except for the use of different molar ratios at the beginning.

For the crystal structures of the obtained HEP samples, $B_{0.9}(\text{FCNZY})_{0.2}$ and $B(\text{FCNZY})_{0.2}$ are in the cubic phase as indicated by the powder XRD patterns in Fig. 1b and further confirmation by the Rietveld refinement of the XRD patterns (Fig. S2) in Table S1. For $B_{0.9}(\text{FCNZY})_{0.2}$, its lattice parameters are $a = b = c = 4.18976$ (46) \AA ($R_p = 4.47\%$, $R_{wp} = 5.66\%$, $\chi^2 = 1.36$), which are similar to those of previously reported perovskite oxides [56]. Compared with that of $B(\text{FCNZY})_{0.2}$, the (110) crystal face of $B_{0.9}(\text{FCNZY})_{0.2}$ shifts to a lower angle (Fig. S3), indicating that crystal expansion has occurred in the presence of A-site non-stoichiometric metal elements; this phenomenon may lead to the creation of additional Fe^{2+} with larger ionic radius than Fe^{3+} (0.645 \AA for Fe^{3+} and 0.780 \AA for Fe^{2+}) [57].

The SEM images of $B_x(\text{FCNZY})_{0.2}$ samples reveal their lava-like porous structures (Fig. 1c, d and Fig. S4) with cavity size at around 300 nm (Fig. S5) that is mainly attributed to the complete decomposition of the randomly distributed chopped oPAN nanofibers. The specific surface areas of $B_x(\text{FCNZY})_{0.2}$ were measured by N_2 adsorption-desorption isotherm and calculated by the BET method to gain insights into the microstructure (Fig. S6). The results showed that all samples exhibit a surface area of $\sim 10^2$ $\text{m}^2 \text{g}^{-1}$, which is larger than that of other typically synthesized perovskite oxides [58]. The pore size distribution results also indicated the existence of meso- and micro-pores in $B_x(\text{FCNZY})_{0.2}$. The homogeneous distributions of different metal elements, including Ba, Fe, Co, Ni, Zr, and Y in $B_x(\text{FCNZY})_{0.2}$

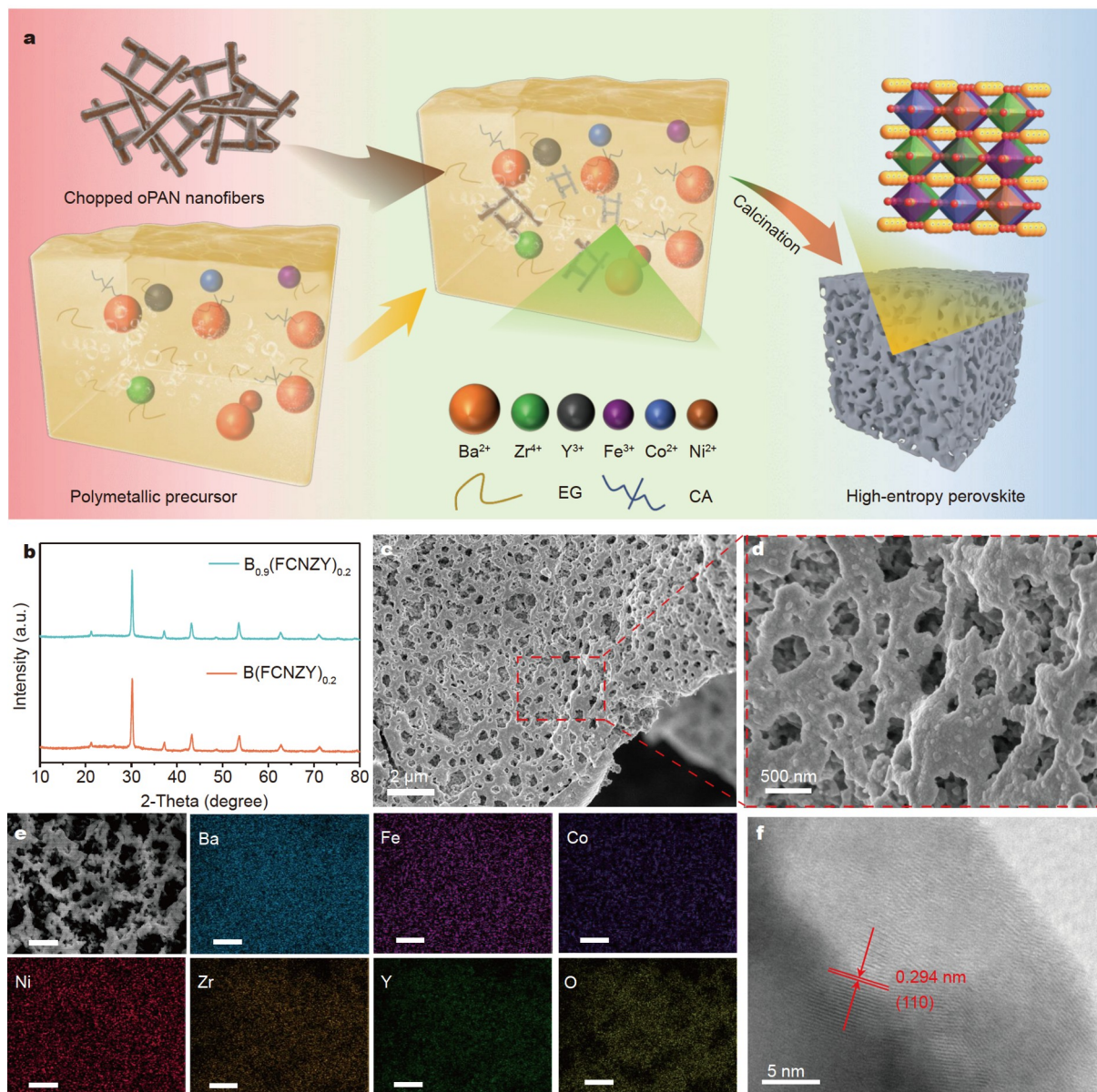


Figure 1 (a) Illustration of the synthesis route for porous lava-like HE perovskite oxide of $B_x(\text{FCNZY})_{0.2}$ ($x = 0.9, 1$). (b) XRD patterns of $B_x(\text{FCNZY})_{0.2}$ ($x = 0.9, 1$). (c, d) SEM images of $B_{0.9}(\text{FCNZY})_{0.2}$. (e) EDX mapping of $B_{0.9}(\text{FCNZY})_{0.2}$ (scale bar: 2 μm). (f) HRTEM image of $B_{0.9}(\text{FCNZY})_{0.2}$.

were confirmed by their corresponding energy-dispersive X-ray (EDX) elemental mappings (Fig. 1e and Fig. S7). Furthermore, the elemental ratios in $B_x(\text{FCNZY})_{0.2}$ were determined by ICP-MS and EDX analysis in Fig. S8, the results of which are in general agreement with the original feed ratios. The measured lattice fringe distances of $B_{0.9}(\text{FCNZY})_{0.2}$ and $B(\text{FCNZY})_{0.2}$ are 0.294 and 0.292 nm, respectively, which correspond to the (110) planes of cubic $B_x(\text{FCNZY})_{0.2}$ (Fig. 1f and Fig. S9). All these results confirmed the successful formation of HEPs for $B(\text{FCNZY})_{0.2}$ and $B_{0.9}(\text{FCNZY})_{0.2}$.

We conducted XPS to investigate the chemical states of different elements. The XPS survey spectra (Fig. S10) confirmed the presence of Ba, Fe, Co, Ni, Zr, Y, and O on $B_x(\text{FCNZY})_{0.2}$ surfaces. No significant signal from the nitrogen element was detected (Fig. S11), thereby excluding the interference of nitrogen sources (mainly from NO_3^-) other than N_2 for eNRR (*vide*

infra). The O 1s spectra of $B(\text{FCNZY})_{0.2}$ and $B_{0.9}(\text{FCNZY})_{0.2}$ were measured to determine the presence of oxygen vacancies. As shown in Fig. 2a, four main characteristic peaks can be observed at ~ 528.7 , ~ 529.6 , ~ 531.1 , and ~ 533.1 eV, which are attributed to lattice O^{2-} , highly oxidative oxygen species ($\text{O}_2^{2-}/\text{O}^-$), surface-adsorbed O_2 or hydroxyl groups, and surface-adsorbed H_2O , respectively [59]. After peak area normalization, the oxygen vacancy ($\text{O}_2^{2-}/\text{O}^-$) content changes from 24.5% for $B(\text{FCNZY})_{0.2}$ to 38.1% for $B_{0.9}(\text{FCNZY})_{0.2}$ (Table S2). Further analysis of the valence states of the six metals (Fig. 2b, Figs S12–S14) showed that the metal at A-position is Ba(+2), and the five metals at the B-position are Fe(+2, +3), Co(+3), Ni(+3), Zr(+4), and Y(+3). For the Ba $3d_{5/2}$ and Co $2p_{3/2}$ spectra in Fig. 2b, distinctive characteristic peaks of Ba^{2+} and Co^{3+} were observed at 779.7 and 778.9 eV, respectively (Table S3) [60]. In addition, the characteristic peaks of Fe (Fig. S12) can be resolved into two peaks at

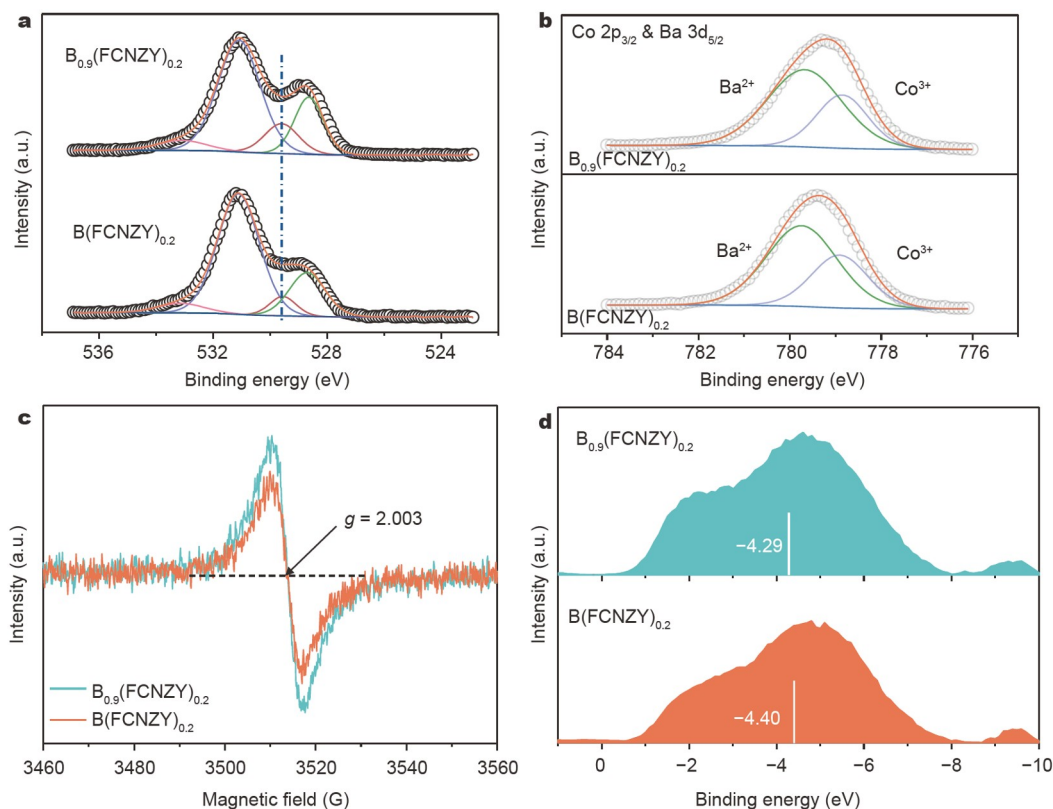


Figure 2 XPS spectra of $B_x(\text{FCNZY})_{0.2}$ ($x = 0.9, 1$): (a) O 1s, (b) Co 2p_{3/2} and Ba 3d_{5/2}. (c) EPR spectra, and (d) surface valence band photoemission spectra of $B_x(\text{FCNZY})_{0.2}$ ($x = 0.9, 1$).

710.4 and 712.9 eV [61], which are assigned to Fe²⁺ and Fe³⁺, respectively. The proportion of Fe³⁺ in B(FCNZY)_{0.2} is higher than that in B_{0.9}(FCNZY)_{0.2} (Table S4), leading to the more positive average valence of iron as Fe(+2.382) in B(FCNZY)_{0.2} than as Fe(+2.367) in B_{0.9}(FCNZY)_{0.2}. Details for the peak splitting of the other three metals (Ni, Zr, and Y) are shown in Figs S13 and S14. The core-level Ni XPS spectra of B_{0.9}(FCNZY)_{0.2} shift to the lower binding energy (~0.3 eV) mainly because the nickel metal valence state decreases when the oxygen vacancy content increases. This finding suggested a redistribution of charge between Ni and O₂²⁻/O⁻ [62,63] that may induce the generation of synergistic active sites and the enhancement of electrical conductivity [64]. Further calculations showed that the valence states of the B-site centers are +3.076 and +3.073 for B(FCNZY)_{0.2} and B_{0.9}(FCNZY)_{0.2}, respectively. These results suggested that the presence of variable metals at the B-site does not play a major role in the formation of oxygen vacancy. As shown in Fig. 2c, B_x(FCNZY)_{0.2} exhibits an EPR signal at $g = 2.003$, which can be identified as electrons trapped in oxygen vacancies. The EPR signal intensity of B_{0.9}(FCNZY)_{0.2} is higher than that of B(FCNZY)_{0.2}, indicating the increase in oxygen vacancy concentration in B_{0.9}(FCNZY)_{0.2} [19]. This finding is in accordance with the XPS O 1s spectra (Fig. 2a). Given that the valence band center of a catalyst directly influences its adsorption of inert gases, such as N₂ [65], the valence band spectra of B_x(FCNZY)_{0.2} are further provided in Fig. 2d. The valence band center of B_{0.9}(FCNZY)_{0.2} (-4.29 eV) is closer to the Fermi energy level than that of B(FCNZY)_{0.2} (-4.40 eV). This result suggested the enhanced adsorption of B(FCNZY)_{0.2} for nitrogen molecules.

Electrochemical activity toward eNRR

Electrochemical tests were carried out on a B_x(FCNZY)_{0.2}/CPE. Prior to the eNRR tests, a series of LSV tests were carried out under N₂- or Ar-saturated 0.1 mol L⁻¹ Li₂SO₄ electrolytes to determine the occurrence of eNRR and the presence of an electroreduction window. As shown in Fig. 3a and Fig. S15a, the current densities in N₂-saturated electrolytes are larger than those in the argon-saturated electrolyte when the working potential is more negative than -0.3 V vs. an RHE, indicating that eNRR mainly occurs below -0.3 V vs. RHE. The time-dependent current density curves for B_x(FCNZY)_{0.2} from -0.3 to -0.8 V were collected every 2 h and are presented in Fig. 3b and Fig. S15b. The NH₃ yield was first measured by the salicylic acid method, and the corresponding calibration curves are shown in Fig. S16. The corresponding ultraviolet-visible (UV-vis) absorption spectra of the electrolytes (stained with indophenol blue indicator) under different working potentials were recorded and are shown in Fig. S17. The best working potential for NH₃ generation is located at -0.6 V. The NH₃ yields and FEs at different potentials are plotted in Fig. 3c, d. Here, we normalized the yield rate of NH₃ production on the basis of the catalyst weight. B_x(FCNZY)_{0.2} exhibits the highest NH₃ yield rate of 24.37 μg h⁻¹ mg⁻¹_{cat} at -0.6 V vs. RHE and the maximum FE at -0.4 V. The FE gradually decreases when the applied potential is more negative than -0.4 V mainly due to the increased dominance of the competing HER. B_{0.9}(FCNZY)_{0.2} exhibits a higher NH₃ yield and FE than B(FCNZY)_{0.2}. The NH₃ yield (24.37 μg h⁻¹ mg⁻¹_{cat} at -0.6 V vs. RHE) and FE (11.70% at -0.4 V vs. RHE) of B_{0.9}(FCNZY)_{0.2} are 1.51 and 1.95 times higher than those of B(FCNZY)_{0.2} (16.11 μg h⁻¹ mg⁻¹_{cat} at

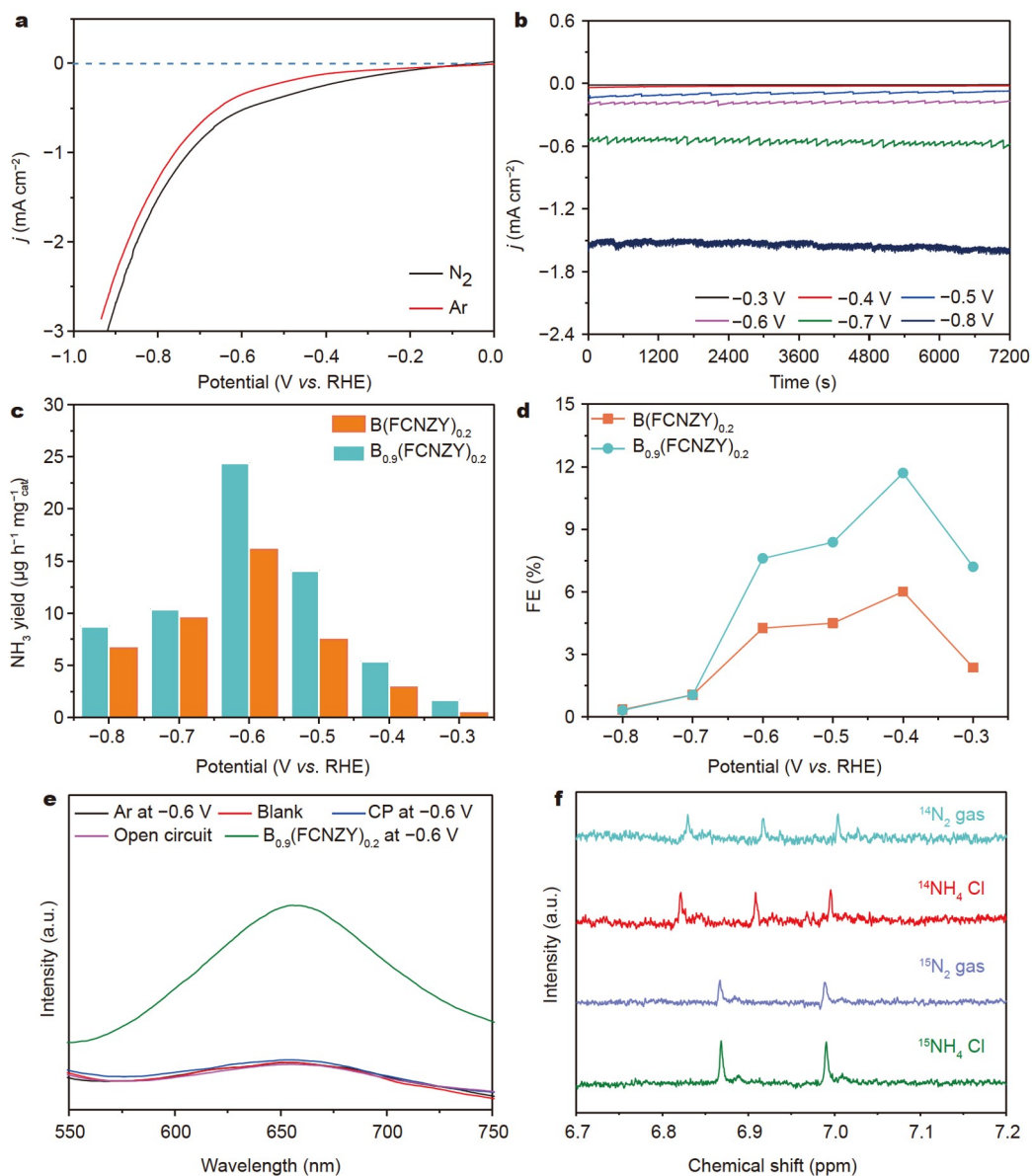


Figure 3 (a) LSV curves in a N_2 - and Ar-saturated 0.1 mol L^{-1} Li_2SO_4 electrolyte. (b) Time-dependent current density curves of $\text{B}_{0.9}(\text{FCNZY})_{0.2}$ at given potentials in the N_2 -saturated 0.1 mol L^{-1} Li_2SO_4 electrolyte. (c) NH_3 yield and (d) FE at each given potential. (e) UV-vis absorption spectra of the $\text{B}_{0.9}(\text{FCNZY})_{0.2}$ electrolytes stained with indophenol indicator under different conditions. (f) ^1H NMR spectra of $^{14}\text{NH}_4^+$ and $^{15}\text{NH}_4^+$ produced by $\text{B}_{0.9}(\text{FCNZY})_{0.2}$ as eNRR electrocatalyst, where $^{14}\text{N}_2$ and $^{15}\text{N}_2$ were used as feeding gases.

-0.6 V, 6.01% at -0.4 V), respectively. These results are comparable to those for the most reported perovskite oxide-based eNRR electrocatalysts (Table S5). For further confirmation, the amount of produced NH_3 was also detected by IC using a standard calibration curve (Fig. S18). The NH_3 yield and FE obtained by the IC method are close to the results from the UV method (Fig. S19). The electrolytes of $\text{B}_x(\text{FCNZY})_{0.2}$ at -0.6 V were also checked for their hydrazine content (Fig. S20), and the results indicated that all the nitrogen consumed in the reduction reaction is converted to NH_3 .

The following control experiments were carried out to prove that the nitrogen in NH_3 is derived from nitrogen gas: (i) carbon paper was used as a working electrode under N_2 -saturated atmosphere, (ii) $\text{B}_{0.9}(\text{FCNZY})_{0.2}$ was tested in Ar-saturated atmosphere, and (iii) $\text{B}_{0.9}(\text{FCNZY})_{0.2}$ was tested in N_2 -saturated atmosphere at an open-circuit configuration. As expected from

the corresponding UV-vis absorption spectra in Fig. 3e, no NH_3 signal was detected. To further confirm that the detected NH_3 has originated from the supplied N_2 , we conducted an experiment using $^{14}\text{N}_2$ and $^{15}\text{N}_2$ as feed gases. The ^1H NMR spectra of commercial $^{14}\text{NH}_4\text{Cl}$ and $^{15}\text{NH}_4\text{Cl}$ samples were obtained as standard spectra and respectively show three peaks and two peaks as displayed in Fig. 3f. These peaks closely match the reference substances ($^{14}\text{NH}_4\text{Cl}$ and $^{15}\text{NH}_4\text{Cl}$) in the region of 6.7–7.2 ppm. No signal of $^{14}\text{NH}_4^+$ was detected in the ^1H NMR spectrum for $^{15}\text{N}_2$, indicating that the synthesized NH_3 is derived from the direct nitrogen supply.

The physical properties of the electrodes can also play an important role during catalysis and can be evaluated by EIS and the determination of the electrochemical active surface area (ECSA) of $\text{B}_x(\text{FCNZY})_{0.2}/\text{CPE}$. As shown in the Nyquist plots in Fig. 4a, $\text{B}_{0.9}(\text{FCNZY})_{0.2}$ with many oxygen vacancies has a lower

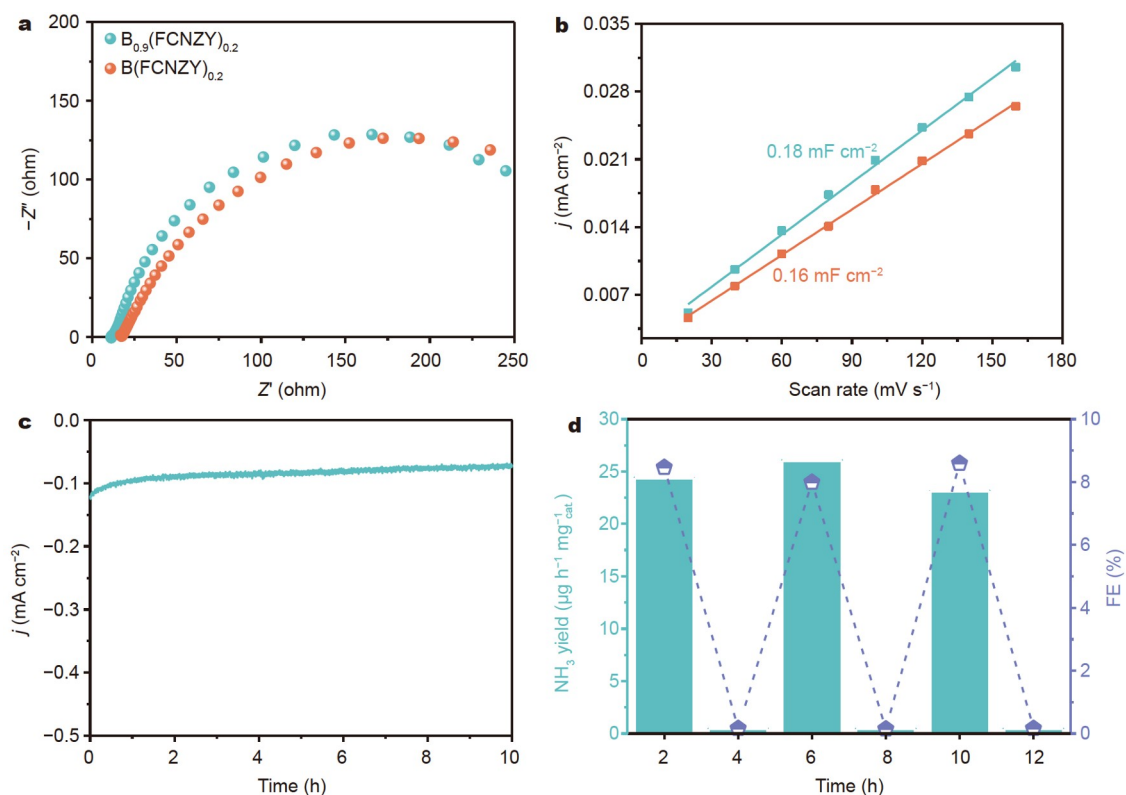


Figure 4 (a) Nyquist plots of $B_x(\text{FCNZY})_{0.2}$ ($x = 0.9, 1$). (b) Charging current density difference plotted against scan rate of $B_x(\text{FCNZY})_{0.2}$. (c) Long-term chronoamperometry curve of $B_{0.9}(\text{FCNZY})_{0.2}$ electrode at -0.6 V vs. RHE in N_2 -saturated electrolyte showing good stability. (d) NH_3 yield rates and corresponding FEs of the $B_{0.9}(\text{FCNZY})_{0.2}$ at -0.6 V with alternating 2 h cycles between N_2 and Ar-saturated electrolytes.

charge transfer resistance and thus a higher electron transfer rate than $B(\text{FCNZY})_{0.2}$ with relatively few oxygen vacancies. To explore the influence of active sites on eNRR, we calculated the ECSAs of $B_x(\text{FCNZY})_{0.2}$ by measuring the C_{dl} (Fig. S21). As shown in Fig. 4b, the C_{dl} of $B_{0.9}(\text{FCNZY})_{0.2}$ is 0.18 mF cm^{-2} , which is nearly equal to that of $B(\text{FCNZY})_{0.2}$ at 0.16 mF cm^{-2} . Moreover, 10 h of eNRR electrocatalysis at -0.6 V has resulted in almost no variation in current density (Fig. 4c), thus further confirming the excellent stability of $B_{0.9}(\text{FCNZY})_{0.2}$ during eNRR. As shown in Fig. S22 and Fig. 4d, positive eNRR behaviors were only obtained for N_2 -saturated electrolytes. Meanwhile, the measurements for Ar-saturated electrolyte were approximated to those for the blank sample, thereby unambiguously confirming that the detected NH_3 has originated from N_2 reduction facilitated by $B_{0.9}(\text{FCNZY})_{0.2}$. Except for the peaks from the CPE substrate, the well-indexed XRD patterns of $B_{0.9}(\text{FCNZY})_{0.2}$ after the cycling test proved its excellent structural stability (Figs S23 and S24). SEM tests were also carried out to further verify the stable morphology during catalysis, and the corresponding images showed that the lava-like structure of $B_{0.9}(\text{FCNZY})_{0.2}$ remains intact after the stability test (Fig. S25).

Mechanism analysis of enhanced eNRR activities

For HE materials, the catalytically active center is difficult to determine from an experimental perspective. Therefore, DFT calculations were conducted to predict the actual sites for the eNRR in $B_{0.9}(\text{FCNZY})_{0.2}$ on the basis of the d-band center theory. The d-band centers for the five elements (Fe, Co, Ni, Zr, and Y) of bulk $B(\text{FCNZY})_{0.2}$ are shown in Fig. S26 and Fig. 5a. Among these elements, the d-band centers of Fe (-6.82 eV), Co

(-6.60 eV), and Ni (-5.43 eV) are closer to the Fermi energy level than those of Zr (-9.81 eV) and Y (-10.11 eV). This finding indicated that nickel, cobalt, and iron are possibly the catalytic active sites in bulk $B(\text{FCNZY})_{0.2}$. After casting the surface based on the HRTEM image (Fig. 2e) and introducing slight vacancies in $B(\text{FCNZY})_{0.2}$ bulk, we constructed a new model of $B_{0.9}(\text{FCNZY})_{0.2}-(110)$, including its electronic structures on the basis of the re-calculated d-band centers of the five metals in Fig. 5a. Ni still displays the closest d-band center of -4.72 eV as compared with the other four metals and thus is the most promising active site for the following eNRR steps. NiO was chosen as a control sample to emphasize the superiority of HEPs. The results showed that the bulk $B_{0.9}(\text{FCNZY})_{0.2}$ exhibits a high eNRR performance (Figs S27 and S28) due to the synergistic effects between nickel and other transition metals. The differential charge diagram further illustrates the activation of N_2 molecules at the oxygen vacancy sites. As shown in Fig. 5b, the Ni atoms near the oxygen vacancies accumulate many electrons, and these localized electrons are subsequently transferred to the adsorbed N_2 molecules.

We calculated the free energy (ΔG) of the intermediates for different eNRR pathways (including the associative distal pathway and the associative alternating pathway) and further determined the optimal reaction path. The structures of the adsorption intermediates are shown in Fig. 5c. For $B_{0.9}(\text{FCNZY})_{0.2}$, the energy barrier (1.61 eV) for $*\text{NHNH} \rightarrow *\text{NHNH}_2$ in the alternating pathway is slightly higher than that for $*\text{NNH}_2 \rightarrow *\text{NNH}_3$ (1.58 eV) in the distal pathway, indicating that the distal pathway is the optimal mechanism for the eNRR of $B_{0.9}(\text{FCNZY})_{0.2}$ catalyst. In addition, the lack of the thermo-

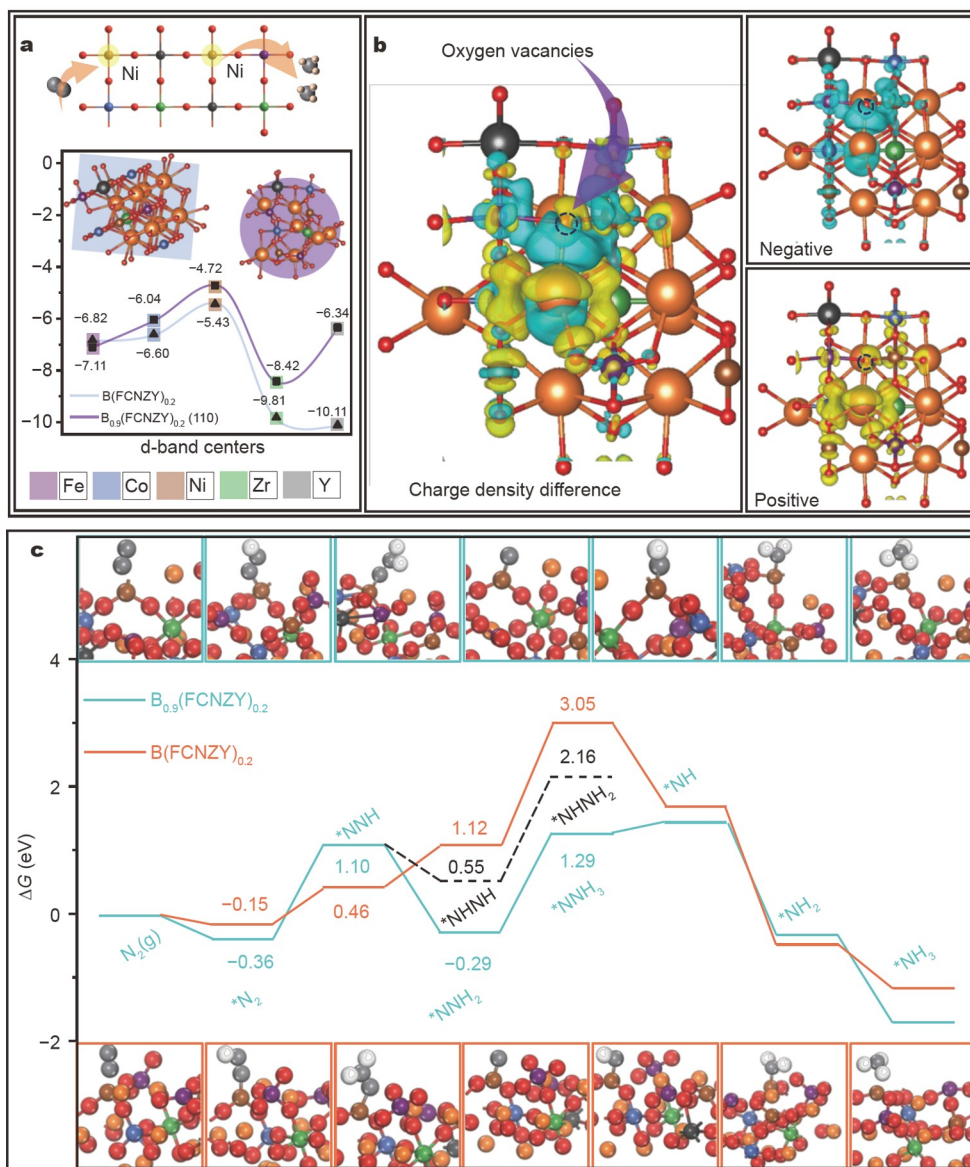


Figure 5 (a) d-Band centers of Fe, Co, Ni, Zr, and Y for B(FCNZY)_{0.2} and B_{0.9}(FCNZY)_{0.2}-(110). (b) Charge density difference induced by oxygen vacancies. (c) Free energy for eNRR on B(FCNZY)_{0.2}-(110) and B_{0.9}(FCNZY)_{0.2}-(110) (solid line for the more favored route and dotted line for the less favored route on the corresponding surface).

dynamically driven intermediate *NHNH₂ provides theoretical evidence on the absence of by-product (NH₂NH₂) in the experiment. By comparing the ΔG values of B_x(FCNZY)_{0.2} catalysts in the associative distal pathway, we found that the third protonation step (*NNH₂ → *NNH₃) is the rate-determining step during the whole eNRR. In particular, B_{0.9}(FCNZY)_{0.2} with additional oxygen vacancies displays a lower energy barrier at 1.58 eV than B(FCNZY)_{0.2} at 1.93 eV. This finding reveals the positive role of the oxygen vacancies in HEPs to accelerate the eNRR.

CONCLUSIONS

In conclusion, we have synthesized a lava-like HEP of formulation B_x(FCNZY)_{0.2} ($x = 0.9, 1$), and its activity has been successfully enhanced using a nonstoichiometric metal element at the A sites. The resulting HEP structures have a high oxygen vacancy concentration. As indicated by DFT calculations, the

nickel element has the greatest potential to act as an active site. The increased concentration of oxygen vacancies facilitates the adsorption of inert N₂ gas, resulting in improved performance. This work provides new design principles for the use of HEP materials in electrocatalytic NH₃ synthesis.

Received 17 January 2022; accepted 2 March 2022;
published online 10 May 2022

- 1 Li P, Jin Z, Fang Z, *et al.* A surface-strained and geometry-tailored nanoreactor that promotes ammonia electrosynthesis. *Angew Chem Int Ed*, 2020, 59: 22610–22616
- 2 Stüeken EE, Kipp MA, Koehler MC, *et al.* The evolution of Earth's biogeochemical nitrogen cycle. *Earth-Sci Rev*, 2016, 160: 220–239
- 3 Wan Y, Xu J, Lv R. Heterogeneous electrocatalysts design for nitrogen reduction reaction under ambient conditions. *Mater Today*, 2019, 27: 69–90
- 4 Nazemi M, Panikkanvalappil SR, El-Sayed MA. Enhancing the rate of electrochemical nitrogen reduction reaction for ammonia synthesis

- under ambient conditions using hollow gold nanocages. *Nano Energy*, 2018, 49: 316–323
- 5 Yesudoss DK, Lee G, Shanmugam S. Strong catalyst support interactions in defect-rich γ - Mo_2N nanoparticles loaded 2D-h-BN hybrid for highly selective nitrogen reduction reaction. *Appl Catal B-Environ*, 2021, 287: 119952
- 6 Zhang L, Liang J, Wang Y, *et al.* High-performance electrochemical NO reduction into NH_3 by MoS_2 nanosheet. *Angew Chem Int Ed*, 2021, 60: 25263–25268
- 7 Li S, Wang Y, Liang J, *et al.* TiB_2 thin film enabled efficient NH_3 electrosynthesis at ambient conditions. *Mater Today Phys*, 2021, 18: 100396
- 8 Fan X, Xie L, Liang J, *et al.* *In situ* grown Fe_3O_4 particle on stainless steel: A highly efficient electrocatalyst for nitrate reduction to ammonia. *Nano Res*, 2022, 15: 3050–3055
- 9 Lai F, Feng J, Ye X, *et al.* Oxygen vacancy engineering in spinel-structured nanosheet wrapped hollow polyhedra for electrochemical nitrogen fixation under ambient conditions. *J Mater Chem A*, 2020, 8: 1652–1659
- 10 Li Z, Ma Z, Liang J, *et al.* MnO_2 nanoarray with oxygen vacancies: An efficient catalyst for NO electroreduction to NH_3 at ambient conditions. *Mater Today Phys*, 2022, 22: 100586
- 11 Wen G, Liang J, Liu Q, *et al.* Ambient ammonia production via electrocatalytic nitrite reduction catalyzed by a CoP nanoarray. *Nano Res*, 2022, 15: 972–977
- 12 Xu T, Liang J, Wang Y, *et al.* Enhancing electrocatalytic N_2 -to- NH_3 fixation by suppressing hydrogen evolution with alkylthiols modified Fe_3P nanoarrays. *Nano Res*, 2022, 15: 1039–1046
- 13 Guo W, Zhang K, Liang Z, *et al.* Electrochemical nitrogen fixation and utilization: Theories, advanced catalyst materials and system design. *Chem Soc Rev*, 2019, 48: 5658–5716
- 14 Lai F, Chen N, Ye X, *et al.* Refining energy levels in ReS_2 nanosheets by low-valent transition-metal doping for dual-boosted electrochemical ammonia/hydrogen production. *Adv Funct Mater*, 2020, 30: 1907376
- 15 Zhao Y, Li F, Li W, *et al.* Identification of M-NH₂-NH₂ intermediate and rate determining step for nitrogen reduction with bioinspired sulfur-bonded few catalyst. *Angew Chem Int Ed*, 2021, 60: 20331–20341
- 16 Cui X, Tang C, Zhang Q. A review of electrocatalytic reduction of dinitrogen to ammonia under ambient conditions. *Adv Energy Mater*, 2018, 8: 1800369
- 17 Suryanto BHR, Du HL, Wang D, *et al.* Challenges and prospects in the catalysis of electroreduction of nitrogen to ammonia. *Nat Catal*, 2019, 2: 290–296
- 18 Chu K, Liu F, Zhu J, *et al.* A general strategy to boost electrocatalytic nitrogen reduction on perovskite oxides via the oxygen vacancies derived from A-site deficiency. *Adv Energy Mater*, 2021, 11: 2003799
- 19 Liu Y, Kong X, Guo X, *et al.* Enhanced N_2 electroreduction over LaCoO_3 by introducing oxygen vacancies. *ACS Catal*, 2020, 10: 1077–1085
- 20 Lai F, Zong W, He G, *et al.* N_2 electroreduction to NH_3 by selenium vacancy-rich ReSe_2 catalysis at an abrupt interface. *Angew Chem Int Ed*, 2020, 59: 13320–13327
- 21 Sim HYF, Chen JRT, Koh CSL, *et al.* ZIF-induced d-band modification in a bimetallic nanocatalyst: Achieving over 44 % efficiency in the ambient nitrogen reduction reaction. *Angew Chem Int Ed*, 2020, 59: 16997–17003
- 22 Yang Y, Wang SQ, Wen H, *et al.* Nanoporous gold embedded ZIF composite for enhanced electrochemical nitrogen fixation. *Angew Chem Int Ed*, 2019, 58: 15362–15366
- 23 Wang M, Liu S, Qian T, *et al.* Over 56.55% Faradaic efficiency of ambient ammonia synthesis enabled by positively shifting the reaction potential. *Nat Commun*, 2019, 10: 341
- 24 Xiong X, Shen D, Zhang Q, *et al.* Achieving high discharged energy density in PVDF-based nanocomposites loaded with fine $\text{Ba}_{0.6}\text{Sr}_{0.4}\text{TiO}_3$ nanofibers. *Compos Commun*, 2021, 25: 100682
- 25 Li C, Ma D, Mou S, *et al.* Porous LaFeO_3 nanofiber with oxygen vacancies as an efficient electrocatalyst for N_2 conversion to NH_3 under ambient conditions. *J Energy Chem*, 2020, 50: 402–408
- 26 Yu J, Li C, Li B, *et al.* A perovskite $\text{La}_2\text{Ti}_2\text{O}_7$ nanosheet as an efficient electrocatalyst for artificial N_2 fixation to NH_3 in acidic media. *Chem Commun*, 2019, 55: 6401–6404
- 27 Hu X, Sun Y, Guo S, *et al.* Identifying electrocatalytic activity and mechanism of $\text{Ce}_{1/3}\text{NbO}_3$ perovskite for nitrogen reduction to ammonia at ambient conditions. *Appl Catal B-Environ*, 2021, 280: 119419
- 28 Zhang S, Duan G, Qiao L, *et al.* Electrochemical ammonia synthesis from N_2 and H_2O catalyzed by doped LaFeO_3 perovskite under mild conditions. *Ind Eng Chem Res*, 2019, 58: 8935–8939
- 29 Ohrelius M, Guo H, Xian H, *et al.* Electrochemical synthesis of ammonia based on a perovskite LaCrO_3 catalyst. *ChemCatChem*, 2020, 12: 731–735
- 30 Zhang H, Xu Y, Lu M, *et al.* Perovskite oxides for cathodic electrocatalysis of energy-related gases: From O_2 to CO_2 and N_2 . *Adv Funct Mater*, 2021, 31: 2101872
- 31 Xu Y, Xu X, Cao N, *et al.* Perovskite ceramic oxide as an efficient electrocatalyst for nitrogen fixation. *Int J Hydrogen Energy*, 2021, 46: 10293–10302
- 32 Chu K, Ras MD, Rao D, *et al.* Tailoring the d-band center of double-perovskite $\text{LaCo}_x\text{Ni}_{1-x}\text{O}_3$ nanorods for high activity in artificial N_2 fixation. *ACS Appl Mater Interfaces*, 2021, 13: 13347–13353
- 33 Yeh JW, Lin SJ, Chin TS, *et al.* Formation of simple crystal structures in Cu-Co-Ni-Cr-Al-Fe-Ti-V alloys with multiprincipal metallic elements. *Metal Mat Trans A*, 2004, 35: 2533–2536
- 34 Wang T, Chen H, Yang Z, *et al.* High-entropy perovskite fluorides: A new platform for oxygen evolution catalysis. *J Am Chem Soc*, 2020, 142: 4550–4554
- 35 Castle E, Csanádi T, Grasso S, *et al.* Processing and properties of high-entropy ultra-high temperature carbides. *Sci Rep*, 2018, 8: 8609
- 36 Jin T, Sang X, Unocic RR, *et al.* Mechanochemical-assisted synthesis of high-entropy metal nitride via a soft urea strategy. *Adv Mater*, 2018, 30: 1707512
- 37 Zhang RZ, Gucci F, Zhu H, *et al.* Data-driven design of ecofriendly thermoelectric high-entropy sulfides. *Inorg Chem*, 2018, 57: 13027–13033
- 38 Gild J, Zhang Y, Harrington T, *et al.* High-entropy metal diborides: A new class of high-entropy materials and a new type of ultrahigh temperature ceramics. *Sci Rep*, 2016, 6: 37946
- 39 Chen H, Jie K, Jafta CJ, *et al.* An ultrastable heterostructured oxide catalyst based on high-entropy materials: A new strategy toward catalyst stabilization via synergistic interfacial interaction. *Appl Catal B-Environ*, 2020, 276: 119155
- 40 Qiao H, Wang X, Dong Q, *et al.* A high-entropy phosphate catalyst for oxygen evolution reaction. *Nano Energy*, 2021, 86: 106029
- 41 Wang T, Fan J, Do-Thanh CL, *et al.* Perovskite oxide-halide solid solutions: A platform for electrocatalysts. *Angew Chem Int Ed*, 2021, 60: 9953–9958
- 42 Ji Q, Bi L, Zhang J, *et al.* The role of oxygen vacancies of ABO_3 perovskite oxides in the oxygen reduction reaction. *Energy Environ Sci*, 2020, 13: 1408–1428
- 43 Jia Z, Gao Z, Kou K, *et al.* Facile synthesis of hierarchical A-site cation deficiency perovskite $\text{La}_x\text{FeO}_{3-y}/\text{RGO}$ for high efficiency microwave absorption. *Compos Commun*, 2020, 20: 100344
- 44 Zhu Y, Chen ZG, Zhou W, *et al.* An A-site-deficient perovskite offers high activity and stability for low-temperature solid-oxide fuel cells. *ChemSusChem*, 2013, 6: 2249–2254
- 45 Tong Y, Wu J, Chen P, *et al.* Vibronic superexchange in double perovskite electrocatalyst for efficient electrocatalytic oxygen evolution. *J Am Chem Soc*, 2018, 140: 11165–11169
- 46 Ren Y, Yu C, Tan X, *et al.* Strategies to suppress hydrogen evolution for highly selective electrocatalytic nitrogen reduction: Challenges and perspectives. *Energy Environ Sci*, 2021, 14: 1176–1193
- 47 Zhu D, Zhang L, Ruther RE, *et al.* Photo-illuminated diamond as a solid-state source of solvated electrons in water for nitrogen reduction. *Nat Mater*, 2013, 12: 836–841
- 48 Watt GW, Chrisp JD. Spectrophotometric method for determination of hydrazine. *Anal Chem*, 1952, 24: 2006–2008
- 49 Kresse G, Furthmüller J. Efficient iterative schemes for *ab initio* total-energy calculations using a plane-wave basis set. *Phys Rev B*, 1996, 54: 11169–11186

- 50 Kresse G, Hafner J. *Ab initio* molecular dynamics for open-shell transition metals. *Phys Rev B*, 1993, 48: 13115–13118
- 51 Kresse G, Furthmüller J. Efficiency of *ab-initio* total energy calculations for metals and semiconductors using a plane-wave basis set. *Comput Mater Sci*, 1996, 6: 15–50
- 52 Ivanov BA, Tartakovskaya EV. Stabilization of long-range magnetic order in 2D easy-plane antiferromagnets. *Phys Rev Lett*, 1996, 77: 386–389
- 53 Blöchl PE. Projector augmented-wave method. *Phys Rev B*, 1994, 50: 17953–17979
- 54 Grimme S, Antony J, Ehrlich S, *et al.* A consistent and accurate *ab initio* parametrization of density functional dispersion correction (DFT-D) for the 94 elements H–Pu. *J Chem Phys*, 2010, 132: 154104
- 55 Zhao J, Chen Z. Single Mo atom supported on defective boron nitride monolayer as an efficient electrocatalyst for nitrogen fixation: A computational study. *J Am Chem Soc*, 2017, 139: 12480–12487
- 56 Ren R, Wang Z, Xu C, *et al.* Tuning the defects of the triple conducting oxide $\text{BaCo}_{0.4}\text{Fe}_{0.4}\text{Zr}_{0.1}\text{Y}_{0.1}\text{O}_{3-\delta}$ perovskite toward enhanced cathode activity of protonic ceramic fuel cells. *J Mater Chem A*, 2019, 7: 18365–18372
- 57 Shannon RD. Revised effective ionic radii and systematic studies of interatomic distances in halides and chalcogenides. *Acta Cryst Sect A*, 1976, 32: 751–767
- 58 She S, Zhu Y, Wu X, *et al.* Realizing high and stable electrocatalytic oxygen evolution for iron-based perovskites by co-doping-induced structural and electronic modulation. *Adv Funct Mater*, 2021, 31: 2111091
- 59 Zhu Y, Zhou W, Yu J, *et al.* Enhancing electrocatalytic activity of perovskite oxides by tuning cation deficiency for oxygen reduction and evolution reactions. *Chem Mater*, 2016, 28: 1691–1697
- 60 Cui X, O’Hayre R, Pylypenko S, *et al.* Fabrication of a mesoporous $\text{Ba}_{0.5}\text{Sr}_{0.5}\text{Co}_{0.8}\text{Fe}_{0.2}\text{O}_{3-\delta}$ perovskite as a low-cost and efficient catalyst for oxygen reduction. *Dalton Trans*, 2017, 46: 13903–13911
- 61 Cong Y, Tang Q, Wang X, *et al.* Silver-intermediated perovskite $\text{La}_{0.9}\text{FeO}_{3-\delta}$ toward high-performance cathode catalysts for nonaqueous lithium-oxygen batteries. *ACS Catal*, 2019, 9: 11743–11752
- 62 Gu J, Li Q, Zheng S, *et al.* $\text{Ni}_{75}\text{Cu}_{25}\text{O}$ polyhedron material derived from nickel-copper oxalate as high-performance electrocatalyst for glucose oxidation. *Compos Commun*, 2022, 29: 100999
- 63 Cheng G, Kou T, Zhang J, *et al.* $\text{O}_2^{2-}/\text{O}^-$ functionalized oxygen-deficient Co_3O_4 nanorods as high performance supercapacitor electrodes and electrocatalysts towards water splitting. *Nano Energy*, 2017, 38: 155–166
- 64 Dai J, Zhu Y, Tahini HA, *et al.* Single-phase perovskite oxide with super-exchange induced atomic-scale synergistic active centers enables ultrafast hydrogen evolution. *Nat Commun*, 2020, 11: 5657
- 65 Wang J, Huang B, Ji Y, *et al.* A general strategy to glassy M–Te (M = Ru, Rh, Ir) porous nanorods for efficient electrochemical N_2 fixation. *Adv Mater*, 2020, 32: 1907112

Acknowledgements This work was supported by the National Natural Science Foundation of China (52161135302, 21674019, and 51801075), the Research Foundation Flanders (G0F2322N), Shanghai Scientific and Technological Innovation Project (18JC1410600), and the Program of the Shanghai Academic Research Leader (17XD1400100). Hofkens J and Martens JA gratefully acknowledge the financial support from the Flemish Government through the Moonshot cSBO project P2C (HBC.2019.0108), the Long-term Structural Funding (Methusalem CASAS2, Meth/15/04) and Interne Fondsen KU Leuven through project C3/20/067. De Ras M gratefully acknowledges the support from the Research Foundation-Flanders (FWO) in the form of a doctoral fellowship (1SA3321N). Chu K gratefully acknowledges the financial support from China Scholarship Council in the form of a visiting Ph.D. Student (File No. 202106790090). Theoretical work was carried out at the LvLiang Cloud Computing Center of China, and the calculations were performed on a TianHe-2 system. We also thank the characterizations supported by the Central Laboratory, School of Chemical and Material Engineering, Jiangnan University.

Author contributions Chu K, Zhang L, Zhang N, Hofkens J, Lai F, and Liu T came up with the concept. Chu K, Qin J, Zhu H, De Ras M, and Xiong L proposed the topic. Chu K, Zhu H, and Xiong L collected the data. Chu K, Qin J, De Ras M, Wang C, Zhang N, and Martens JA analyzed the data. Chu K wrote the original draft. All authors contributed to the general discussion.

Conflict of interest The authors declare that they have no conflict of interest.

Supplementary information Supporting data are available in the online version of the paper.



Kaibin Chu received his BE and MS at Jiangnan University. He is currently a PhD student in Tianxi Liu’s group at the School of Chemical and Material Engineering, Jiangnan University. His research focuses on the design of inorganic perovskite materials for electrocatalytic ammonia synthesis.



Feili Lai received his BS degree from Donghua University (2014), master’s degree from Fudan University (2017), and PhD degree from Max Planck Institute of Colloids and Interfaces/Universität Potsdam (2019). He is now a research fellow of the Department of Chemistry, KU Leuven. His current interests include machine learning in materials science, and the design and synthesis of low-dimensional solids for energy storage and conversion applications.



Tianxi Liu received his BS degree from Henan University (1992) and PhD degree from the Changchun Institute of Applied Chemistry, Chinese Academy of Sciences (1998). He is currently a full professor at Jiangnan University. His main research interests include polymer nanocomposites, organic/inorganic hybrid materials, nanofibers and their composites, advanced energy materials and energy conversion and storage.

高熵钙钛矿氧化物: 一种应用于氮气还原的通用材料

楚凯斌¹, 秦静静¹, 朱海燕¹, Michiel De Ras², 王闯², 熊磊³, 张龙生¹, 张楠¹, Johan A. Martens⁴, Johan Hofkens^{2,5}, 赖飞立^{2*}, 刘天西^{1*}

摘要 在过去的几年里, 电催化氮还原反应(eNRR)吸引了大量的研究兴趣。尽管如此, NH_3 的产量和选择性仍然没有达到实际应用的标准。本论文报道了成分为 $\text{Ba}_x(\text{FeCoNiZrY})_{0.2}\text{O}_{3-\delta}$ ($\text{B}_x(\text{FCNZY})_{0.2}$ ($x = 0.9, 1$))的高熵钙钛矿作为eNRR催化剂的新材料研究平台。通过改变A位金属元素的非化学计量比, 使材料产生更高密度的氧缺陷, 进而提升氮气还原性能。 $\text{B}_{0.9}(\text{FCNZY})_{0.2}$ 的 NH_3 产率和法拉第效率是 $\text{B}(\text{FCNZY})_{0.2}$ 的1.51和1.95倍。理论上, 利用d-带中心理论预测了B-位点的催化活性中心, 并确定了镍元素为催化位点。最佳远端反应途径中的中间状态的自由能值表明, 第三个质子化步骤($*\text{NNH}_2 \rightarrow *\text{NNH}_3$)是决定速率的步骤, 高熵钙钛矿氧化物中氧空位的增加对氮的吸附和还原都有贡献。这项工作作为具有多个活性位点的高熵结构应用于电催化固氮提供了一个新的研究框架。